

Collisions of Deformed Nuclei: A Path to the Far Side of the Superheavy Island

Akira Iwamoto[†], Peter Möller^{†‡§¶}, J. Rayford Nix[¶], and Hiroyuki Sagawa[‡]

[†]Advanced Science Research Center, Japan Atomic Energy Research Institute, Tokai, Nakagun, Ibaraki, 319-11 Japan

[‡]Center for Mathematical Sciences, University of Aizu, Aizu-Wakamatsu, Fukushima 965-80, Japan

[§]P. Moller Scientific Computing and Graphics, Inc., P. O. Box 1440, Los Alamos, NM 87544, USA

[¶]Theoretical Division, Los Alamos National Laboratory, Los Alamos, NM 87545, USA

Abstract. A detailed understanding of complete fusion cross sections in heavy-ion collisions requires a consideration of the effects of the deformation of the projectile and target. Our aim here is to show that deformation and orientation of the colliding nuclei have a very significant effect on the fusion-barrier height and on the compactness of the touching configuration. To facilitate discussions of fusion configurations of deformed nuclei, we develop a classification scheme and introduce a notation convention for these configurations. We discuss particular deformations and orientations that lead to compact touching configurations and to fusion-barrier heights that correspond to fairly low excitation energies of the compound systems. Such configurations should be the most favorable for producing superheavy elements. We analyze a few projectile-target combinations whose deformations allow favorable entrance-channel configurations and whose proton and neutron numbers lead to compound systems in a part of the superheavy region where α half-lives are calculated to be observable, that is, longer than 1 μ s.

1. Introduction

The last five elements that have been discovered [1–5] were all formed in cold-fusion reactions between spherical nuclei. As the proton number increases, the cross section for heavy-element production decreases. For example, element 107 was produced with a 167 pb cross section [1], whereas for element 111 the production cross section was only 2–3 pb [5]. There is reason to suspect that few additional new elements can be reached in reactions between spherical nuclei because of the strong decreasing trend of the cross sections.

In a fusion reaction several processes influence the evaporation-residue cross section σ_{er} for heavy-element formation. One may write

$$\begin{aligned}\sigma_{\text{cn}} &= \sigma_{\text{fus}}(1 - P_{\text{ff}}) \\ \sigma_{\text{er}} &= \sigma_{\text{cn}}(1 - P_{\text{cf}})\end{aligned}\tag{1}$$

Here σ_{cn} is the cross section for forming a compound nucleus, σ_{fus} is the fusion cross section corresponding to the coalescence of the target and projectile, P_{ff} is the probability for fast fission prior to forming a compound system, and P_{cf} is the probability for fission during the deexcitation of the compound nucleus through neutron and gamma emission.

In fusion reactions where the number of protons in the projectile and target add up to about 100, the overwhelming inelastic cross-section component is fusion-fission, which includes both processes in which the coalesced system undergoes fast fission prior to compound-nucleus formation and the compound nucleus undergoes fission before complete deexcitation. For bombarding energies close to the Coulomb barrier σ_{fus} is in the millibarn range, whereas σ_{er} is in the picobarn range. Because small changes in the fusion-reaction parameters and the nuclear-structure parameters may change P_{ff} and P_{cf} by orders of magnitude but leave σ_{fus} essentially unchanged when the incident energy measured from the barrier top is the same, σ_{fus} is relatively unimportant in heavy-element formation. Instead, it is crucial to minimize P_{ff} and P_{cf} , which are very close to 1 in reactions leading to compound systems with more than 200 nucleons.

In general, large negative shell corrections of the ground state of the compound system decrease P_{cf} and consequently enhance the heavy-element-formation cross section σ_{er} . The compound-nucleus fission cross section is usually modeled in terms of a level-density formalism.

Models for P_{ff} are much less reliable than models for P_{cf} . In a classical picture a necessary condition for complete fusion and the formation of a compound nucleus is that the fusing system evolves into a configuration inside the fission saddle point in a multi-dimensional deformation space [6–9]. In heavy-ion collisions where the projectile and target are of roughly equal size and with a nucleon number A above about 100, the touching configuration lies on the side of a steep hill outside the fission saddle point [10]. For energies just above the Coulomb barrier this topographical feature results in a trajectory that is deflected away from the direction that would lead to the spherical shape. Instead, it proceeds from the touching configuration to the fission valley, so that no compound-nucleus formation occurs.

There are two simple possibilities for overcoming the above limitation to compound-nucleus formation and increasing the cross section for heavy-element production. First, if the projectile energy is increased sufficiently high, the trajectory will in the absence of dissipative forces pass inside the fission saddle point. However, dissipation may make such trajectories difficult to realize. Second, highly asymmetric touching configurations may be sufficiently close to the ground-state shape of the compound nucleus that the touching configuration is inside the fission saddle point. Thus, these two simple principles would suggest that to produce elements in the superheavy region one should select highly asymmetric configurations and increase the projectile energy above the Coulomb barrier. However, high excitation energies and the resulting high angular momentum of the compound system may favor fission instead of de-excitation by neutron emission. In the cold-fusion approach that led to the identification of the five heaviest elements, the very nature of cold fusion leads to a low excitation energy of the compound system. The entrance-channel configuration is also fairly asymmetric and compact. However, the maximum cross section for the production of the heaviest elements occurs at sub-barrier energies as very rare, non-classical events.

In our study here we will mainly argue that in the fusion of deformed nuclei there are particular deformations and relative orientations of the target and projectile that favor compound-nucleus formation, that is, decrease P_{ff} . Our discussion above revealed that from very general principles one can expect that heavy-element production in heavy-ion reactions is most favorable when the touching configuration is compact. The excitation energy of the compound system should be high enough to allow a trajectory inside the fission saddle point, but otherwise as low as possible to reduce the fission branch of the compound system. A spherical picture of nuclei in heavy-ion collisions allows few new possibilities for very-heavy-element production beyond what has already been accomplished. It is therefore of interest to investigate if consideration of deformation will identify entrance-channel configurations that have some possibility of being more favorable for heavy-element production than is expected from the spherical

picture. To facilitate the discussion of deformed fusion configurations we introduce a classification scheme, notation and terminology.

2. Fusion configurations of deformed nuclei: Classification, notation and terminology

Obviously, the multi-dimensional fusion potential is a continuous function of the incident direction and orientation of the projectile nucleus and of the deformation of the projectile and target. However, to allow the identification and discussion of major physical effects it is useful to identify and study a few limiting situations.

2.1. Limiting fusion configurations

Our discussion of specific cases below will show that for prolate shapes there are significant differences in the fusion process depending on the sign of the hexadecapole moment. Nuclei with a large negative hexadecapole moment develop a neck which allows a close approach. As a result the fusion configuration for some orientations of the projectile-target combinations is considerably more compact than the corresponding configurations for shapes with large positive hexadecapole moments. Thus, we identify four limiting situations as far as deformations are concerned. They are:

1. Well-developed oblate shapes
2. Spherical shape
3. Well-developed prolate shapes with large negative hexadecapole moments Q_4
4. Well-developed prolate shapes with large positive hexadecapole moments Q_4

Furthermore, we assume mass symmetry and axial symmetry as this is consistent with the vast majority of nuclear ground-state configurations.

In our studies here we use alternatively the Nilsson perturbed-spheroid parameterization ϵ [11] and the β parameterization to generate deformed nuclear shapes. In the β parameterization, assuming axial symmetry, the radius vector $R(\theta, \phi)$ to the nuclear surface is defined by

$$R(\theta, \phi) = R_0 \left[1 + \sum_{l=1}^{\infty} \beta_l Y_l^0(\theta, \phi) \right] \quad (2)$$

where R_0 is deformation dependent so as to conserve the volume inside the nuclear surface. The variation in R_0 due to volume conservation is only a fraction of one percent. The definition of the ϵ parameterization is more complicated. A recent, extensive presentation is given in Ref. [12]. One should note that large positive Q_4 corresponds to positive β_4 but to negative ϵ_4 and that large negative Q_4 corresponds to negative β_4 but to positive ϵ_4 .

As limiting orientations we consider only situations where the projectile center is on the x, y or z axis of the target and orientations of the projectile where the projectile symmetry axis is either parallel to or perpendicular to the target symmetry axis. Since we restrict ourselves to axial symmetry, configurations with the projectile center located on the x or y axis are identical. If the projectile is located in the equatorial region of the target it can be oriented in three major orientations, and if it is located in the polar region it can be oriented in two major orientations. Thus, for a particular projectile-target deformation combination there are five possible limiting configurations.

Because there are five orientations and three major types of deformations for both projectile and target there are 45 different configurations when the projectile and target are deformed and of unequal

mass. When the projectile and target are of equal mass, one would at first sight expect 30 different configurations. We later show that in the case of equal projectile and target mass there are three pairs of configurations where the two configurations in the pairs are identical. Therefore, there are in this case only 27 deformed configurations that are different. Situations where either the projectile or target is deformed add another six configurations and, finally, we designate a spherical target and a spherical projectile as a separate configuration. Thus, in our classification scheme we find 34 configurations of projectile and target in heavy-ion collisions that are different also in the special case of equal projectile and target mass. For the case of unequal projectile and target mass one may wish to count a total of 45 different deformed configurations, for a total of 52 different fusion configurations.

We will in a separate study systematically review the barrier parameters of these configurations for projectiles and targets throughout the periodic system. Here, we will just discuss a few configurations with potential importance for very-heavy-element production. However, to be able to simply and transparently refer to any of the limiting configurations we start by introducing a notation convention for deformed fusion configurations.

2.2. Notation for deformed fusion configurations

We denote a particular fusion configuration by [P,T,O], where the three letters stand for Projectile deformation, Target deformation, and relative Orientation of the projectile-target combination. For configurations where the projectile or target or both are spherical, the number of different limiting orientations is less than when both the projectile and target are deformed. It is therefore most clear to introduce notation that distinguishes between these possibilities. The following values are possible for the three entities P, T and O:



P and T

Oblate:.....	o
Spherical	s
Prolate with negative Q_4	p^-
Prolate with positive Q_4	p^+






O Spherical projectile and spherical target

Spherical (s)	
---------------------	---

O Spherical-deformed projectile-target combination

Polar (p)	
Equatorial (e)	

O Deformed-deformed projectile-target configuration

Polar-transverse (pt)	
Polar-parallel (pp)	
Equatorial-transverse (et)	
Equatorial-parallel (ep)	
Equatorial-cross (ec)	

We prefer the graphical short-hand notation given in the table above for the different orientations, but we also provide in parenthesis an alternative notation, based on letters only.

In Fig. 1 we show the seven different configurations that can occur with a spherical projectile. We have sandwiched the familiar spherical-projectile spherical-target case between the prolate-target and oblate-target configurations in the top row so that the appearance of the configurations evolves smoothly from the polar, spherical-prolate positive-hexadecapole configuration $[s,p^-, \overset{\circ}{|}]$ on the extreme left to the polar, spherical-projectile oblate-target configuration $[s,o, \overset{\circ}{|}]$ on the far right.

In Figs. 2–10 we show the 45 different configurations occurring in our scheme when both the projectile and target are deformed and of unequal mass. In the case of equal projectile and target mass the configuration $[p^+, p^-, \top]$ and $[p^-, p^+, -]$, for example, are identical. Indeed, in this case all the configurations $[p^-, p^+, \text{any}]$ have a corresponding configuration $[p^+, p^-, \text{any}]$, and other similar correspondences also occur. Therefore, when the projectile and target mass are equal, one need not consider any configuration that occurs in Figs. 5, 8 and 9 because equivalent configurations will have occurred in an earlier figure. For equal-mass projectile-target combinations the configurations $[p^+, p^+, \top]$, $[p^-, p^-, \top]$ and $[o, o, \top]$ are equivalent to $[p^+, p^+, -]$, $[p^-, p^-, -]$ and $[o, o, -]$, respectively. This is the reason there are only 27 different configurations when the projectile and target are of equal mass.

In Figs. 1–10 we use the β parameterization to describe the nuclear shape. Volume conservation has not been applied in these and subsequent figures of nuclear shapes, but this is an insignificant approximation since volume conservation only changes R_0 by fractions of a percent for the deformations considered. However, in energy calculations it is essential to include volume conservation, as we do in our calculations here. As representative deformations we make the following choices. As the prolate–positive hexadecapole deformation p^+ we choose $\beta_2 = 0.30$ and $\beta_4 = 0.11$. This corresponds to the experimentally determined deformation of ^{154}Sm [12]. The prolate–negative hexadecapole deformation p^- is chosen as $\beta_2 = 0.24$ and $\beta_4 = -0.09$, corresponding to the experimentally determined deformation of ^{186}W [12]. Finally, as a representative oblate deformation we have selected $\beta_2 = -0.25$ and $\beta_4 = 0.0$. The ratio between R_0 of the projectile and target is 0.7.

3. Deformation and heavy-ion collisions

Although the implications of deformation on cross sections for superheavy-element production have not been very extensively considered so far, deformation certainly is already known to affect fusion cross sections leading to somewhat lighter compound systems. For example, a clear signature of the importance of deformation effects in heavy-ion reactions is the enhancement of sub-barrier fusion cross sections, for which deformation often plays a major role. It may be useful to observe that the designation sub-barrier is somewhat of a misnomer. An implicit assumption behind this designation is that both projectile and target nuclei are spherical. Furthermore, if the measured cross section at energies below the maximum of this assumed spherical fusion barrier is higher than the calculated cross section for this configuration then the term *enhanced sub-barrier fusion* is used. In a more realistic picture one can in many cases show that (1) the energy is not sub-barrier and (2) the measured cross section is not enhanced. To illustrate these features we select the reaction $^{16}\text{O} + ^{154}\text{Sm}$.

3.1. Deformation and the fusion potential-energy surface

We show in Fig. 11 a calculated fusion potential-energy surface for the reaction $^{16}\text{O} + ^{154}\text{Sm}$. The potential-energy surface is calculated in our previously developed model [12] for the macroscopic potential energy between two arbitrarily oriented, deformed heavy ions. The potential shown in Fig. 11 is considerably simpler than the most general case, since the projectile is spherical and the target has both mass and axial symmetry. Thus, for this system the fusion potential is completely specified by this two-dimensional figure.

We present in Table 1 four fusion-barrier quantities for particular orientations between the projectile and target. Each line corresponds to one orientation and one incident direction. The first eight columns specify the projectile and target nuclei and the deformation used for these nuclei in the calculation of the fusion barrier. The shapes of the projectile and target are given in the Nilsson perturbed-spheroid parameterization [11]. The next column gives the relative orientation of projectile and target in the notation introduced above. The last four columns indicate (1) the distance between the centers-of-mass of the projectile and target at the maximum of the barrier, (2) the maximum of the fusion barrier, (3)

Table 1. Comparison of entrance-channel fusion configurations. When the sign $<$ is given in the column for R_{\max} and $>$ is given in the column for V_{\max} it means that the maximum of the fusion barrier occurs inside the touching point and consequently is higher than the potential of the touching configuration.

	Target			Projectile				Barrier				
	ϵ_2	ϵ_4	ϵ_6		ϵ_2	ϵ_4	ϵ_6	Or.	R_{\max} (fm)	V_{\max} (MeV)	R_t (fm)	V_t (MeV)
^{154}Sm	0.000	0.000	0.000	^{16}O	0.000	0.000	0.000	\odot	10.54	62.21	9.14	56.22
^{154}Sm	0.250	-0.067	0.030	^{16}O	0.000	0.000	0.000	d	10.10	63.29	8.80	57.90
^{154}Sm	0.250	-0.067	0.030	^{16}O	0.000	0.000	0.000	\circ	11.87	57.18	10.67	53.34
^{150}Nd	0.000	0.000	0.000	^{150}Nd	0.000	0.000	0.000	\odot	$<$	$>$	12.33	379.10
^{150}Nd	0.225	-0.067	0.025	^{150}Nd	0.225	-0.067	0.025	$+$	$<$	$>$	11.74	390.96
^{150}Nd	0.225	0.200	-0.100	^{150}Nd	0.225	0.200	-0.100	$+$	11.69	399.51	10.29	383.98
^{150}Nd	0.225	0.100	-0.044	^{150}Nd	0.225	0.100	-0.044	$+$	11.66	396.73	10.86	392.38
^{186}W	0.208	0.100	-0.044	^{110}Pd	0.200	0.027	-0.013	\top	$<$	$>$	12.29	358.13
^{186}W	0.208	0.100	-0.044	^{110}Pd	0.200	0.027	-0.013	\mid	$<$	$>$	13.46	342.61
^{186}W	0.208	0.100	-0.044	^{110}Pd	0.200	0.027	-0.013	\vdash	$<$	$>$	12.15	359.01
^{186}W	0.208	0.100	-0.044	^{110}Pd	0.200	0.027	-0.013	\parallel	11.69	375.12	10.99	372.84
^{186}W	0.208	0.100	-0.044	^{110}Pd	0.200	0.027	-0.013	$+$	11.69	376.20	10.99	374.14
^{186}W	0.000	0.000	0.000	^{110}Pd	0.000	0.000	0.000	\odot	$<$	$>$	12.18	361.10
^{192}Os	0.142	0.073	-0.032	^{104}Ru	0.233	-0.013	0.012	$+$	11.72	367.82	11.22	367.11
^{186}W	0.208	0.100	-0.044	^{104}Ru	0.233	-0.013	0.012	$+$	11.54	362.33	10.94	360.95
^{186}W	0.208	0.100	-0.044	^{116}Cd	-0.233	0.053	-0.002	\mid	12.44	379.14	11.84	377.30
^{186}W	0.208	0.100	-0.044	^{116}Cd	-0.233	0.053	-0.002	\vdash	11.44	397.59	10.54	391.47
^{186}W	0.000	0.000	0.000	^{116}Cd	0.000	0.000	0.000	\odot	$<$	$>$	12.28	375.27
^{248}Cm	0.217	-0.013	0.042	^{48}Ca	0.000	0.000	0.000	\circ	13.31	198.33	12.41	195.44
^{248}Cm	0.217	-0.013	0.042	^{48}Ca	0.000	0.000	0.000	d	11.69	212.56	11.09	211.23

the center-of-mass distance when the projectile and target just touch and (4) the fusion-barrier height at this point.

The first three lines of Table 1 show fusion-barrier data for the reaction $^{16}\text{O} + ^{154}\text{Sm}$. In the first line of the table we show, for reference, the calculated barrier parameters for a hypothetical spherical target shape. The second line gives the fusion-barrier parameters for the configuration [s,p⁺,d] corresponding to the equatorial plane $z = 0$ in Fig. 11 and the third line corresponds to the potential in the [s,p⁺, \circ] configuration, that is, to the line $\rho = 0$ in Fig. 11.

3.2. Deformation and fusion cross sections

In Fig. 12 the measured and calculated fusion cross sections corresponding to the fusion potential-energy surface displayed in Fig. 11 are presented. Figure 12 is taken from a calculation [13] of fusion cross sections in reactions of spherical projectiles and deformed targets. It has no free parameters except a simple translation in energy of the calculated cross-section curves. The cross section is obtained by integrating over angle the transmission coefficients which are determined by calculating the barrier penetrability at each angular momentum by use of the WKB approximation. The deformed fusion potential is obtained in a model calculation with no free parameters and is the sum of the nuclear and Coulomb potentials according to Ref. [12] and a centrifugal barrier term, which is treated in the spherical limit. The deformation parameters of the target are taken from a recent calculation of nuclear ground-state masses

and deformations [14]. Obviously, there are large deformation effects both in the potential energy and in the fusion cross section. Our model, incorporating significant aspects of deformation, accounts well for the “enhancement” of the cross section relative to the fusion cross section obtained for a hypothetical spherical target, at least for energies down to the Coulomb barrier in the polar direction.

However, our present model of fusion cross sections does not account for fusion enhancement due to surface vibrations. For example, it cannot account for the well-known enhancements in fusion cross sections in such reactions as $^X\text{Ni} + ^Y\text{Ni}$ of Ni isotopes, where X and Y are close to 58. A recent study of such reactions is found in Ref. [15].

To further illustrate aspects of our unified approach to calculating nuclear ground-state masses, shapes, reaction and decay Q values, β -decay rates, fission barriers, and fusion cross section σ_{fus} we discuss some similarities and differences between our fusion cross section calculation and a recent, detailed study [16] of the reaction $^{16}\text{O} + ^{154}\text{Sm}$ and other reactions. The latter study is based on a parameterized distribution of fusion barriers, where deformation and several other parameters are selected so as to obtain optimum agreement with data. In our calculation the nuclear and Coulomb potentials are generated from *calculated* nuclear ground-state shapes. The parameters of our potentials are identical to those of a global nuclear mass calculation [17,18]. The only free parameter in our fusion cross-section calculation is a translation of the calculated curve, corresponding to an adjustment of the calculated fusion-barrier height. In our calculation we take into account the three lowest even multipole shape deformations and evaluate the integral expressions for the Coulomb and nuclear interaction energies by numerical integration to obtain the required accuracy. In contrast, the study of Ref. [16] considers only β_2 and β_4 shape parameters and the Coulomb interaction is evaluated only approximately by expanding to order β_2^2 and β_4 .

Despite some differences between our calculation and that of Ref. [16], the similarities are substantial. In particular, we are in good agreement with their conclusions about the values of the deformation parameters β_2 and β_4 for ^{154}Sm and agree with Ref. [16] that earlier ambiguities about the values of these deformation parameters as derived from fusion cross-section data were largely due to inexact theoretical models for the fusion cross sections. We obtain a difference of 6.56 MeV between the fusion-barrier height in the equatorial and polar regions, whereas Ref. [16] obtains a difference of 8 MeV.

Many other calculations of the fusion cross section for the reaction $^{16}\text{O} + ^{154}\text{Sm}$ have been published earlier. In most of these studies a set of nuclear deformation parameters are determined by adjusting the calculated curve to the measured cross-section values. Our purpose in presenting our calculated cross section for this reaction here is to show that our cross-section calculation based on *calculated* deformation parameters agrees extremely well with the measured values. Thus, our *calculated* nuclear shape of ^{154}Sm should closely resemble the actual shape. Because of this very good agreement, our discussions below of the influence of higher multipole moments on P_{ff} can be expected to be based on realistic ground-state deformations. It has been shown earlier [19] that the sign of β_4 significantly influences the fusion cross section σ_{fus} . Because changing the sign of β_4 under certain conditions may influence P_{ff} by several orders of magnitude but influences σ_{fus} much less, we are below mainly concerned with how quadrupole and higher multipole deformations affect P_{ff} . One should note that increasing ϵ_4 while keeping ϵ_2 fixed decreases the fusion cross section, whereas, as we argue below, it can be expected to increase compound-nucleus-formation probability or equivalently decrease P_{ff} . The effect of ϵ_4 variations on P_{ff} is under certain circumstances expected to be substantially larger than the (opposite) effect on σ_{fus} , so that there is an overall increase in the evaporation-residue cross section σ_{er} for increasing ϵ_4 .

3.3. Gentle fusion?

Because the evaporation-residue cross sections in cold fusion between spherical projectiles and targets drop so strongly towards heavier nuclei, Nörenberg [20,21] suggested that “gentle fusion” of two well-deformed rare-earth nuclei in an equatorial-cross orientation \dagger should be investigated because, he stated, “this orientation leads to the most compact touching configuration out of all possible orientations of the

two deformed nuclei.” Consequently, the evaporation-residue cross sections may be sufficiently large to allow detection.

We first observe that according to our calculations [14], only the lightest nuclei in the rare-earth region would lead to compound systems with α half-lives over 1 μ s, which is the approximate transit time from the target to detection area in the SHIP experimental setup. Already the reaction $^{160}\text{Gd} + ^{160}\text{Gd} \rightarrow ^{320-xn}128 + xn$ leads to nuclei where the calculated [14,22] α -decay half-lives are less than about 0.01 μ s. To study the concept of gentle fusion we must therefore select a reaction in the beginning of the rare-earth region, so we choose the reaction $^{150}\text{Nd} + ^{150}\text{Nd}$ to illustrate Nörenberg’s suggestion. We show the configuration of two ^{150}Nd nuclei with calculated ground-state shapes in Fig. 13. The configuration is $[\text{p}^+, \text{p}^+, +]$ and is the one proposed by Nörenberg as favorable for SHE production. Calculated fusion-barrier data for the hypothetical spherical case and the configuration in Fig. 13 are found in Table 1, on lines 4 and 5, respectively.

It is clear that the fusion configuration $+$ suggested by Nörenberg is limited to $[\text{p}^+, \text{p}^+, +]$ configurations, since projectiles and targets must be chosen from the beginning of the rare-earth region. This configuration is not particularly compact relative to a collision between similar-size spherical nuclei, as is clear from Figs. 2 and 13 and Table 1. Indeed, because of the large negative ϵ_4 of the ground state, which results in a bulging equatorial region and a large positive hexadecapole moment, the configuration in Fig. 13 is quite similar to the spherical configuration. This observation is supported by the quantitative results in Table 1: the distance between mass centers of the gentle fusion configuration is 11.74 fm, only 0.59 fm more compact than the spherical configuration.

The idea that configurations where deformed nuclei touch each other in the equatorial regions are more compact than some other configurations and may therefore be favorable for SHE production is not new. It was for instance mentioned in Ref. [12] in a discussion of the reaction $^{48}\text{Ca} + ^{248}\text{Cm}$, and we will return to this reaction below. Clearly, the fusion barrier for deformed systems along a one-dimensional path will be very different in the polar direction and in an equatorial direction. When the projectile is deformed the fusion barrier will also depend strongly on the orientation of the incident deformed projectile.

It is obvious that when colliding heavy ions have well-developed prolate deformation, then the most compact configurations occur when the point of touching is in the equatorial region of both nuclei. Which relative orientation of the two nuclei, $+$ or $||$, is the most favorable is perhaps not known at present. However, the orientation suggested by Nörenberg is one possible favorable configuration, but its properties will depend strongly on the value of the hexadecapole deformation, that is, in our case on the value of the deformation parameter ϵ_4 . Large negative values of ϵ_4 correspond to bulging equatorial regions, whereas positive values lead to neck formation. We now look at the latter, more compact configurations.

3.4. *Hugging fusion!*

To clearly illustrate the effect of large positive values of the deformation parameter ϵ_4 we first study an example where we for clarity exaggerate somewhat the effect. We show in Fig. 14 the configuration in Fig. 13, with one change, namely we select ϵ_4 and ϵ_6 so that a well-developed neck results. The configuration is $[\text{p}^-, \text{p}^-, +]$. The corresponding calculated fusion-barrier parameters are listed on line 6 of Table 1. This hypothetical shape is presented to show the effect of a well-developed neck on the fusion barrier and touching configuration. Clearly this configuration is very different from both the spherical configuration and the gentle configuration and quite compact. Similar configurations with necks in the equatorial regions instead of bulging midsections could favor a large cross section for complete fusion. Because the nuclei “grab” each other we call this configuration corresponding to this specific orientation and where both projectile and target exhibit some neck formation *hugging fusion*. In our classification scheme hugging fusion corresponds to the $[\text{p}^-, \text{p}^-, +]$ class of touching fusion configurations. The ϵ_4 deformation value selected to clearly show this principle is probably unrealistically large. However, large positive ϵ_4 deformations occur in the end of the rare-earth region. To compare the effect of a realistic

positive value of ϵ_4 with the effect of a large negative ϵ_4 we apply the deformation calculated [14] for ^{186}W to ^{150}Nd and display the configuration in Fig. 15 and the fusion barrier in line 7 of Table 1. We see that the distance between mass centers of this configuration is only 10.86 fm, that is, 1.47 fm more compact than the spherical configuration and 0.88 fm more compact than a configuration with a large negative ϵ_4 . To exploit the enhancement of the evaporation-residue cross section that we expect in the hugging configuration $[\text{p}^-, \text{p}^-, +]$ we must find suitable projectiles and targets with large positive ϵ_4 ground-state deformations that lead to superheavy elements with half-lives that are sufficiently long that the evaporation residues are observable.

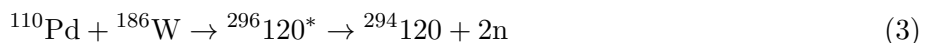
4. Heavy-ion reactions for distant superheavy-element production

The most stable nuclei on the superheavy island are predicted to occur in the vicinity of $^{288-294}110$ even though the magic proton number in this region is calculated to be 114 [22]. However, nuclei at some considerable distance away from the center of the island are calculated to be sufficiently long-lived to allow observation after formation; that is, they are predicted to have half-lives in excess of 1 μs . We refer to elements with proton number larger than 114 as distant superheavy elements. We now look at some heavy-ion reactions that may lead to this far part of the superheavy island.

4.1. Hugging fusion candidates for distant superheavy-element production

Above we noted that to achieve very compact configurations of deformed nuclei one should find projectiles and targets with large positive values of the ϵ_4 deformation parameter. Clearly then, the best candidates for a stable target above proton number 50 would be nuclei near the end of the rare-earth region. To be specific, we select ^{186}W as a target in our first example. For this nucleus, calculations [14] give $\epsilon_4 = 0.100$ and $\epsilon_6 = -0.044$. The large negative value of ϵ_6 also contributes to the development of a neck. A suitable projectile that would take us to the region of distant superheavy elements would then be ^{110}Pd leading to the compound system $^{296}120$. The hugging configuration for this choice is shown from four different angles in Fig. 16. The fusion barrier for the hugging configuration $[\text{p}^-, \text{p}^-, +]$ is listed on line 12 of Table 1, where we to illustrate the orientation effect on the fusion barrier also list the barrier parameters for the four other deformed configurations $[\text{p}^-, \text{p}^-, \top]$, $[\text{p}^-, \text{p}^-, |]$, $[\text{p}^-, \text{p}^-, \perp]$ and $[\text{p}^-, \text{p}^-, ||]$ on lines 8–11. These five deformed configurations also appear in Fig. 6 for slightly different projectile-target sizes and deformations. The table listing on lines 8–12 is in the order the configurations occur in Fig. 6. In Table 1 we also list on line 13, for reference, the barrier parameters for the $[\text{s}, \text{s}, \circ]$ configuration.

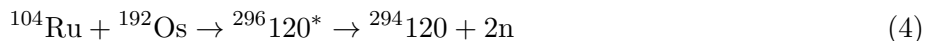
To make an estimate of the decay properties of the compound system we make the following assumptions. The heavy-ion reaction takes place at the fusion-barrier energy. We do not calculate the branching ratio between fusion-fission and complete fusion, but are primarily interested in studying the alpha-decay rates of the compound nuclei that possibly do not fission but de-excite by neutron emission. One expects of course that at high excitation energy some washing out of shell effects has taken place and that Γ_f/Γ_n is large. It is a remaining, important problem to calculate this quantity. We assume that neutrons are emitted as long as energetically possible. The Q -values and masses required for these calculations are obtained from Ref. [14]. The α -decay half-lives are calculated as discussed in Ref. [22]. With these assumptions we find for the reaction and configuration $[\text{p}^-, \text{p}^-, +]$ shown in Fig. 16 at a center-of-mass energy equal to the Coulomb barrier energy listed on line 12 in Table 1 that two neutrons are emitted. Thus



where the compound nucleus has an excitation energy of 35.04 MeV before neutron emission. The α -decay-chain half-lives and Q -values are shown in Fig. 17. Although the first few decays are calculated to be only a few μs , these decays should be within the detection limit of SHIP. Fission half-life calculations are characterized by large uncertainties [22], but the calculated ground-state microscopic corrections in

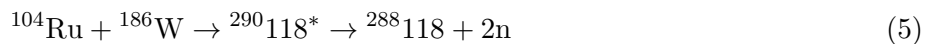
the region of the compound system are about -7 MeV, so one expects a fission barrier about this high in this region of nuclei. Such a high barrier would probably be associated with fission half-lives that are longer than the calculated α half-lives down to about element 104 for all the decay chains considered here.

We have also considered the reaction



The barrier parameters are listed on line 14 in Table 1. A beam energy equal to the Coulomb barrier value of 367.82 MeV leads to a compound-nucleus excitation energy of 34.06 MeV, which is about 1 MeV lower than in the reaction (3), and consequently to the same α -decay sequence after 2n emission.

We have also calculated the fusion-barrier parameters for the $[p^-, p^-, +]$ configuration of the reaction



with the result that the compound system $^{290}118$ is created at an excitation energy of 38.67 MeV for a beam energy at the Coulomb barrier, leading to 2n emission. The barrier parameters are listed on line 15 in Table 1. The resulting α -decay chain is two neutrons more deficient than the reaction (3) and is shown in Fig. 18.

4.2. Oblate fusion configurations

We showed above that the sign of ϵ_4 significantly influenced fusion-barrier properties of colliding heavy ions. Correspondingly, one anticipates that the sign of ϵ_2 has a large effect on the fusion barrier, so in Figs. 19 and 20 we give two examples of fusion configurations corresponding to an oblate projectile and a prolate target for the reaction



We have taken the ground-state deformations from the mass calculation of Ref. [14]. Experimentally the sign of the ground-state quadrupole deformation is sometimes not known and may be different from the calculated value. The examples in this section are therefore intended only as examples of how oblate deformations affect fusion properties. The corresponding barrier parameters, as well as the parameters for the spherical reference case are listed on lines 16–18 in Table 1. Because the configuration $[o, p^-, |]$ shown in Fig. 19 resembles a Japanese Kokeshi doll, although our head here is somewhat large, we call this configuration as well as the configuration $[o, p^+, |]$ Kokeshi. The Kokeshi configuration is somewhat more compact than the spherical case at a cost of only a marginally higher barrier. The configuration shown in Fig. 20 is considerably more compact than the Kokeshi configuration, but at the cost of an 18 MeV higher fusion barrier. The calculated neutron-emission and α -decay chains of the compound nuclei corresponding to the initial configurations in Figs. 19 and 20 are shown in Figs. 21 and 22, respectively. For both orientations we have chosen the beam energy as the Coulomb barrier listed for the configuration in Table 1.

4.3. An earlier favorite

Because the reaction



leads to a compound system near the doubly magic $^{298}114$ in the superheavy region, and because the asymmetric entrance-channel configuration was thought to enhance the evaporation-residue cross section it was a favorite reaction in the past. However, several experiments at different beam energies based on this reaction did not lead to the identification of any evaporation residues in the superheavy region

[23]. This reaction involves a spherical projectile and a deformed target. Thus, there are two limiting orientations, polar and equatorial, which are shown in Figs. 23 and 24, respectively, with the corresponding fusion-barrier parameters listed on lines 19 and 20 of Table 1. From the figures and table it is clear that the equatorial configuration $[s, p^+, d]$ is much more compact than the polar configuration $[s, p^+, |]$ and consequently the equatorial configuration should be the most favorable for heavy element-production. Although several beam energies in the range between the polar and equatorial Coulomb barriers were investigated in the experiments [23] there are several possibilities why no heavy elements were observed.

First, the cross-section limit at which detection was possible was several orders of magnitude higher than the limits that have been achieved today.

Second, in cold fusion there is appreciable cross section only in a narrow range, a few MeV, of beam energy [4]. Also in hot fusion the beam energy may be critically important and it is not clear that any of the beam energies in the experiment [23] corresponded to maximum cross section, in particular since no accurate theoretical model exists for the evaporation-residue cross section as a function of beam energy and nuclear orientation. If compact fusion configurations are favorable one would in analogy with cold fusion suspect that one should choose a beam energy slightly below the Coulomb barrier in the equatorial direction. We show in Fig. 25 the α -decay chain that is calculated to occur from the compound system after neutron emission, when the compound system is formed in a $[s, p^+, d]$ configuration at a beam energy corresponding to the Coulomb barrier in this direction.

Third, the rare cold-fusion events that lead to heavy-element formation have been described in terms of *fusion initiated by transfer* (FIT) [24]. In this description the occupancy of levels near the Fermi surface suggests that nucleons will transfer from target to projectile, resulting in increasing Coulomb repulsion. In the FIT model one therefore expects a very low evaporation-residue cross section for this reaction [24].

5. Summary

In heavy-ion collisions between deformed projectiles and targets we have shown that the fusion reaction depends strongly on the relative orientation of the projectile and target. Both the fusion-barrier height and the compactness of the touching configuration are so strongly affected that a variation of relative orientation may have a similar impact as varying the projectile and/or target nuclear species. Therefore, a detailed consideration of deformation is necessary in both theory and experimental work so that we can understand more about the many features of heavy-ion reactions between deformed nuclei. To facilitate such studies we have introduced a classification scheme of deformed fusion configurations.

Systematic experimental work on understanding cold-fusion reactions and associated cross sections for evaporation-residue formation and parallel investigations of microscopic nuclear-structure models have over the last 20 years or so led to the discovery of five new elements on the side of the superheavy island closest to us. Similar or more extensive work will be required to describe in detail the fusion reactions between two deformed nuclei. However, the reward may be access to the far side of the superheavy island. Of particular interest is to study how the high charge numbers of these nuclei affect nuclear and atomic properties. Above we have given a few examples of heavy-ion reactions that could serve as particularly suitable starting points for exploring both theoretically and experimentally the new physics of deformed heavy-ion reactions, and possibly the new physics of the far side of the superheavy island. In particular we have suggested that a few special fusion configurations may be especially favorable for forming superheavy elements. In hot fusion, we suggest as most favorable an asymmetric projectile-target combination in the *hugging* configuration $[p^-, p^-, +]$.

This work was supported by the Japan Atomic Energy Research Institute and by the U. S. Department of Energy.

References

- [1] G. Münzenberg, S. Hofmann, F. P. Heßberger, W. Reisdorf, K.-H. Schmidt, J. R. H. Schneider, P. Armbruster, C.-C. Sahn, and B. Thuma, *Z. Phys.* **A300** (1981) 7.
- [2] G. Münzenberg, P. Armbruster, H. Folger, F. P. Heßberger, S. Hofmann, J. Keller, K. Poppensieker, W. Reisdorf, K.-H. Schmidt, H. J. Schött, M. E. Leino, and R. Hingmann, *Z. Phys.* **A317** (1984) 235.
- [3] G. Münzenberg, P. Armbruster, F. P. Heßberger, S. Hofmann, K. Poppensieker, W. Reisdorf, J. R. H. Schneider, W. F. W. Schneider, K.-H. Schmidt, C.-C. Sahn, and D. Vermeulen, *Z. Phys.* **A309** (1982) 89.
- [4] S. Hofmann, N. Ninov, F. P. Heßberger, P. Armbruster, H. Folger, G. Münzenberg, H. J. Schött, A. G. Popeko, A. V. Yeremin, A. N. Andreyev, S. Saro, R. Janik, and M. Leino, *Z. Phys.* **A350** (1995) 277.
- [5] S. Hofmann, N. Ninov, F. P. Heßberger, P. Armbruster, H. Folger, G. Münzenberg, H. J. Schött, A. G. Popeko, A. V. Yeremin, A. N. Andreyev, S. Saro, R. Janik, and M. Leino, *Z. Phys.* **A350** (1995) 281.
- [6] J. R. Nix and A. J. Sierk, *Phys. Scr.* **10A** (1974) 94.
- [7] J. R. Nix and A. J. Sierk, *Phys. Rev.* **C15** (1977) 2072.
- [8] J. Błocki, Y. Boneh, J. R. Nix, J. Randrup, M. Robel, A. J. Sierk, and W. J. Swiatecki, *Ann. Phys. (N. Y.)* **113** (1978) 330.
- [9] K. T. R. Davies, A. J. Sierk, and J. R. Nix, *Phys. Rev.* **C28** (1983) 679.
- [10] P. Möller and J. R. Nix, *Nucl. Phys.* **A272** (1976) 502.
- [11] S. G. Nilsson, *Kgl. Danske Videnskab. Selskab. Mat.-Fys. Medd.* **29**:No. 16 (1955).
- [12] P. Möller and A. Iwamoto, *Nucl. Phys.* **A575** (1994) 381.
- [13] A. Iwamoto and P. Möller, to be published (1995).
- [14] P. Möller, J. R. Nix, W. D. Myers, and W. J. Swiatecki, *Atomic Data Nucl. Data Tables* **59** (1995) 185.
- [15] A. M. Stefanini, D. Ackermann, L. Corradi, D. R. Napoli, C. Petrache, P. Spolare, P. Bednarczyk, H. Q. Zhang, S. Beghini, G. Montagnoli, L. Mueller, F. Scarlassara, G. F. Segato, F. Soramel, and N. Rowley, *Phys. Rev. Lett.* **74** (1995) 864.
- [16] R. J. Leigh, N. Rowley, R. C. Lemmon, D. J. Hinde, J. O. Newton, J. X. Wei, J. C. Mein, C. R. Morton, S. Kuyucak, and A. T. Kruppa, *Phys. Rev.* **C47** (1993) 47.
- [17] P. Möller and J. R. Nix, *Nucl. Phys.* **A361** (1981) 117.
- [18] P. Möller and J. R. Nix, *Atomic Data Nucl. Data Tables* **26** (1981) 165.
- [19] R. C. Lemmon, R. J. Leigh, J. X. Wei, C. R. Morton, D. J. Hinde, J. O. Newton, J. C. Mein, M. Dasgupta, and N. Rowley, *Phys. Lett.* **B316** (1993) 32.
- [20] W. Nörenberg, *Proc. Int. Workshop on Heavy-Ion Fusion, Padua, Italy* (1994).
- [21] W. Nörenberg, *GSI Nachrichten 10-94 (Oct. 1994)* p. 13.
- [22] P. Möller and J. R. Nix, *J. Phys. G: Nucl. Part. Phys.* **20** (1994) 1681.
- [23] P. Armbruster, Y. K. Agarwal, W. Bröchle, M. Brügger, J. P. Dufour, H. Gäggeler, F. P. Heßberger, S. Hofmann, P. Lemmert, G. Münzenberg, K. Poppensieker, W. Reisdorf, M. Schädel, K.-H. Schmidt, J. R. H. Schneider, W. F. W. Schneider, K. Sümmerer, D. Vermeulen, G. Wirth, A. Ghiorso, K. E. Gregorich, D. Lee, M. E. Leino, K. J. Moody, G. T. Seaborg, R. B. Welch, P. Wilmarth, S. Yashita, C. Frink, N. Greulich, G. Herrmann, U. Hickmann, N. Hildebrand, J. V. Kratz, N. Trautmann, M. M. Fowler, D. C. Hoffman, W. R. Daniels, H. R. von Gunten, and H. Dornhöfer, *Phys. Rev. Lett.* **54** (1985) 406.
- [24] S. Hofmann, *Proc. XV Nuclear Physics Divisional Conf. on 'Low Energy Nuclear Dynamics,' St. Petersburg, Russia* (1995).
- [25] R. G. Stokstad, Y. Eisen, S. Kaplanis, D. Pelte, U. Smilansky, and I. Tserruya, *Phys. Rev.* **C21** (1980) 2427.

Figure Captions

- Fig. 1 The seven limiting touching configurations with spherical projectiles. The simplest configuration with a spherical target is in the top row third from the left. To the left of this configuration are configurations with prolate target shapes whereas to the right are the two limiting configurations that occur for oblate target shape. The ratio between the projectile and target volume is 0.343. The deformation is $\beta_2 = 0.30$ and $\beta_4 = 0.11$ for p^+ , $\beta_2 = 0.24$ and $\beta_4 = -0.09$ for p^- , and $\beta_2 = -0.25$ and $\beta_4 = 0.0$ for o shapes. The arrows give the direction of the incident beam. The nuclear symmetry axis is indicated by a thin line emerging from the nuclear polar regions.
- Fig. 2 Five limiting touching configurations with prolate, positive-hexadecapole projectiles and targets. Specifically $\beta_2 = 0.30$ and $\beta_4 = 0.11$. The ratio between the projectile and target volume is 0.343. Only the relative positions and orientations change between the configurations. The arrows give the direction of the incident beam. The nuclear symmetry axis is indicated by a thin line emerging from the nuclear polar regions.
- Fig. 3 Five limiting touching configurations with a prolate, positive-hexadecapole projectile and a prolate, negative-hexadecapole target. Specifically, for the projectile $\beta_2 = 0.30$ and $\beta_4 = 0.11$ and for the target $\beta_2 = 0.24$ and $\beta_4 = -0.09$. The ratio between the projectile and target volume is 0.343. Only the relative positions and orientations change between the configurations. The arrows give the direction of the incident beam. The nuclear symmetry axis is indicated by a thin line emerging from the nuclear polar regions.
- Fig. 4 Five limiting touching configurations with a prolate, positive-hexadecapole projectile and an oblate target. Specifically, for the projectile $\beta_2 = 0.30$ and $\beta_4 = 0.11$ and for the target $\beta_2 = -0.25$ and $\beta_4 = 0$. The ratio between the projectile and target volume is 0.343. Only the relative positions and orientations change between the configurations. The arrows give the direction of the incident beam. The nuclear symmetry axis is indicated by a thin line emerging from the nuclear polar regions.
- Fig. 5 Five limiting touching configurations with a prolate, negative-hexadecapole projectile and a prolate, positive-hexadecapole target. Specifically, for the projectile $\beta_2 = 0.24$ and $\beta_4 = -0.09$ and for the target $\beta_2 = 0.30$ and $\beta_4 = 0.11$. The ratio between the projectile and target volume is 0.343. Only the relative positions and orientations change between the configurations. The arrows give the direction of the incident beam. The nuclear symmetry axis is indicated by a thin line emerging from the nuclear polar regions.
- Fig. 6 Five limiting touching configurations with prolate, negative-hexadecapole projectiles and targets. Specifically $\beta_2 = 0.24$ and $\beta_4 = -0.09$. The ratio between the projectile and target volume is 0.343. Only the relative positions and orientations change between the configurations. The arrows give the direction of the incident beam. The nuclear symmetry axis is indicated by a thin line emerging from the nuclear polar regions.
- Fig. 7 Five limiting touching configurations with a prolate, negative-hexadecapole projectile and an oblate target. Specifically, for the projectile $\beta_2 = 0.24$ and $\beta_4 = -0.09$ and for the target $\beta_2 = -0.25$ and $\beta_4 = 0$. The ratio between the projectile and target volume is 0.343. Only the relative positions and orientations change between the configurations. The arrows give the direction of the incident beam. The nuclear symmetry axis is indicated by a thin line emerging from the nuclear polar regions.
- Fig. 8 Five limiting touching configurations with an oblate projectile and a prolate, positive-hexadecapole target. Specifically, for the projectile $\beta_2 = -0.25$ and $\beta_4 = 0.0$ and for the

target $\beta_2 = 0.30$ and $\beta_4 = 0.11$. The ratio between the projectile and target volume is 0.343. Only the relative positions and orientations change between the configurations. The arrows give the direction of the incident beam. The nuclear symmetry axis is indicated by a thin line emerging from the nuclear polar regions.

- Fig. 9 Five limiting touching configurations with an oblate projectile and a prolate, negative-hexadecapole target. Specifically, for the projectile $\beta_2 = -0.25$ and $\beta_4 = 0.0$ and for the target $\beta_2 = 0.24$ and $\beta_4 = -0.09$. The ratio between the projectile and target volume is 0.343. Only the relative positions and orientations change between the configurations. The arrows give the direction of the incident beam. The nuclear symmetry axis is indicated by a thin line emerging from the nuclear polar regions.
- Fig. 10 Five limiting touching configurations with oblate projectiles and targets. Specifically, $\beta_2 = -0.25$ and $\beta_4 = 0$. The ratio between the projectile and target volume is 0.343. Only the relative positions and orientations change between the configurations. The arrows give the direction of the incident beam. The nuclear symmetry axis is indicated by a thin line emerging from the nuclear polar regions.
- Fig. 11 Calculated potential-energy surface in units of MeV for the reaction $^{16}\text{O} + ^{154}\text{Sm}$. The energy in the medium-gray area, outside the dark-grey ^{154}Sm nucleus in the center was not calculated, because the points in this region correspond to points inside the touching configuration. The light-gray shape inside the ^{154}Sm nucleus has been drawn to show the relative size of the projectile to the target. This overlapping configuration is not considered in actual calculations. Note the ridge with saddle points and peaks around the target nucleus.
- Fig. 12 Calculated fusion cross sections for the reaction $^{16}\text{O} + ^{154}\text{Sm}$, compared to experimental data [25]. The solid curve corresponds to the fusion surface shown in Fig. 11 when the shape of the target corresponds to the calculated ground-state shape. The long-dashed curve is the cross section obtained for a hypothetical spherical target. The arrows show the fusion-barrier height in the polar direction (p), the equatorial plane (e), and the barrier height for a hypothetical spherical target (s). Both the curves and the arrows have been translated in energy by $E_{\text{tran}} = -3.1$ MeV from their calculated values.
- Fig. 13 Touching configuration of $^{150}\text{Nd} + ^{150}\text{Nd}$ with the nuclear shapes taken to be the calculated [14] ground-state shape; that is, the configuration is $[\text{p}^+, \text{p}^+, +]$. The arrow gives the direction of the incident beam. Fusion-barrier parameters for this configuration/direction are given on line 5 of Table 1.
- Fig. 14 Touching configuration of $^{150}\text{Nd} + ^{150}\text{Nd}$ for hypothetical nuclear shapes with a large positive ϵ_4 and a choice of ϵ_6 that further develops the waistline; that is, the configuration is $[\text{p}^-, \text{p}^-, +]$. The arrow gives the direction of the incident beam. Fusion-barrier parameters for this configuration/direction are given on line 6 of Table 1.
- Fig. 15 Touching configuration of $^{150}\text{Nd} + ^{150}\text{Nd}$ for shapes corresponding to a realistic ground-state shape in the rare earth region; that is, the configuration is $[\text{p}^-, \text{p}^-, +]$. Specifically, we have chosen the ground-state shape parameters of ^{186}W . Fusion-barrier parameters for this configuration/direction are given on line 7 of Table 1.
- Fig. 16 Touching configuration of $^{110}\text{Pd} + ^{186}\text{W}$ for calculated ground-state shapes viewed from four different angles. The shapes used are the calculated ground-states shapes, so the configuration is $[\text{p}^-, \text{p}^-, +]$. The arrows and \otimes sign give the direction of the incident beam. Fusion-barrier parameters for this configuration/direction are given on line 12 of Table 1.

- Fig. 17 Calculated Q -values for α decay and corresponding calculated half-lives for the decay chain starting at $^{294}_{120}$.
- Fig. 18 Calculated Q -values for α decay and corresponding calculated half-lives for the decay chain starting at $^{288}_{118}$.
- Fig. 19 Polar-parallel Kokeshi configuration of $^{116}\text{Cd} + ^{186}\text{W}$ for shapes corresponding to calculated ground-state deformation parameters; that is, the configuration is $[o, p^-, \cdot]$. The arrow gives the direction of the incident beam. Fusion-barrier parameters for this configuration/direction are given on line 16 of Table 1.
- Fig. 20 Equatorial-transverse configuration of $^{116}\text{Cd} + ^{186}\text{W}$ for shapes corresponding to calculated ground-state deformation parameters; that is, the configuration is $[o, p^-, -]$. The arrow gives the direction of the incident beam. Fusion-barrier parameters for this configuration/direction are given on line 17 of Table 1.
- Fig. 21 Calculated Q -values for α decay and corresponding calculated half-lives for the decay chain starting at $^{301}_{122}$.
- Fig. 22 Calculated Q -values for α decay and corresponding calculated half-lives for the decay chain starting at $^{300}_{122}$.
- Fig. 23 Touching configuration of $^{48}\text{Ca} + ^{248}\text{Cm}$ for shapes corresponding to calculated ground-state deformation parameters. The arrow gives the direction of the incident beam. Fusion-barrier parameters for this configuration/direction are given on line 19 of Table 1.
- Fig. 24 Touching configuration of $^{48}\text{Ca} + ^{248}\text{Cm}$ for shapes corresponding to calculated ground-state deformation parameters. The arrow gives the direction of the incident beam. Fusion-barrier parameters for this configuration/direction are given on line 20 of Table 1.
- Fig. 25 Calculated Q -values for α decay and corresponding calculated half-lives for the decay chain starting at $^{293}_{116}$.

- 1.
- 2.
- 3.
- 4.
- 5.
- 6.
- 7.
- 8.
- 9.
- 10.
- 11.
- 12.
- 13.
- 14.
- 15.
- 16.
- 17.
- 18.
- 19.
- 20.
- 21.
- 22.
- 23.
- 24.
- 25.